

See discussions, stats, and author profiles for this publication at: <https://www.researchgate.net/publication/228552924>

# The Dielectric Function of Silver Nanoparticle Langmuir Monolayers Compressed through the Metal Insulator Transition

ARTICLE *in* JOURNAL OF THE AMERICAN CHEMICAL SOCIETY · MAY 2000

Impact Factor: 12.11 · DOI: 10.1021/ja991543f

CITATIONS

53

READS

18

## 5 AUTHORS, INCLUDING:



**Sven E. Henrichs**

Intel

13 PUBLICATIONS 925 CITATIONS

SEE PROFILE



**Charles Patrick Collier**

Oak Ridge National Laboratory

80 PUBLICATIONS 6,146 CITATIONS

SEE PROFILE



**Richard J Saykally**

University of California, Berkeley

460 PUBLICATIONS 28,078 CITATIONS

SEE PROFILE



**yi-ren Shen**

China Medical University (ROC)

249 PUBLICATIONS 10,375 CITATIONS

SEE PROFILE

# The Dielectric Function of Silver Nanoparticle Langmuir Monolayers Compressed through the Metal Insulator Transition

S. Henrichs,<sup>†</sup> C. P. Collier,<sup>†</sup> R. J. Saykally,<sup>‡</sup> Y. R. Shen,<sup>§</sup> and J. R. Heath<sup>\*,†</sup>

Contribution from the Department of Chemistry and Biochemistry, University of California, Los Angeles, 405 Hilgard Avenue, Los Angeles, California 90095-1569, and Departments of Chemistry and Physics, University of California, Berkeley, California 94045

Received May 10, 1999

**Abstract:** Algorithms and experimental techniques for extracting the complex dielectric function of thin films (monolayers and bilayers) of quantum dots are developed. The algorithms are based on a combination of the so-called Newton–Raphson method, used in conjunction with a Kramers–Kronig analysis, and are used to analyze normal-incidence reflectance and transmission measurements of organically passivated silver quantum dot Langmuir monolayers. Single, unambiguous solutions to the dielectric function were determined for several particle monolayers and at various stages of compression. A transition of the quantum dot superlattice from the insulating to a metallic state was observed. When a monolayer of 6-nm-diameter Ag nanocrystals is compressed to an interparticle separation distance of  $\sim 8\text{--}9\text{ \AA}$ , a negative-valued featureless component of the real part of the dielectric function is detected. This indicates the onset of Drude-like behavior that is characteristic of a metallic film. The impact of superlattice disorder on this Drude response is also investigated.

## I. Introduction

The optical properties of quantum dot superlattices contain information concerning the nature and strength of interparticle coupling within the superlattice. Although there are a large number of papers reporting on the photoluminescence,<sup>1</sup> absorbance, and/or reflectance<sup>2</sup> from quantum dot solids,<sup>3</sup> there have not been any reports on the complex optical dielectric function of such materials. In this paper, we present an approach toward determining the optical dielectric function of Langmuir monolayer superlattices of silver quantum dots, measured as a function of monolayer compression. We include a description of the experimental measurements techniques, as well as the algorithms that we utilized to determine a single, unambiguous solution of the dielectric function from experimental reflectance and transmittance measurements.

We recently demonstrated that it was possible to *reversibly* tune a monolayer of hexagonally packed, organically functionalized 3-nm-diameter silver quantum dots (QDs) through the metal–insulator (MI) transition using the Langmuir compression technique.<sup>4</sup> We presented this work as an example of rational engineering of a specific electronic property into a QD solid.<sup>5</sup> At large interparticle separation distances, the superlattice is a Mott insulator,<sup>6</sup> with a Coulomb band gap described by the

charging energies of the individual nanoparticle lattice sites.<sup>7,8</sup> Upon compression, the Coulomb gap disappears and the density of states (DOS) becomes temperature-independent (down to 20 K) and finite-valued at the Fermi level.<sup>9</sup> After the transition to the metal phase, the superlattice should be characterized by free electrons, and that behavior should be reflected in the frequency-dependent complex optical dielectric function ( $\epsilon(\omega) = \epsilon_1(\omega) + i\epsilon_2(\omega)$ ) of the superlattice.

We previously showed that, at low frequencies (10 kHz–10 MHz),  $\epsilon_1(\omega)$  switches from a positive- to a negative-valued function, indicating the onset of a Drude response, or free electron behavior within the superlattice.<sup>10</sup> The results presented here are measurements of this same function, but at much higher frequencies, and represent the first *quantitative* measurements of this MI transition. These results, therefore, allow us to make comparisons to both theory and related systems, such as evaporated Ag island films as they pass through the percolation transition.<sup>11</sup> In addition, we find evidence to support the prediction by Levine and Remacle of a disorder-induced insulating film that exists between the Mott insulator and the metallic phase.<sup>12</sup> This localized phase has also been directly observed in recent tunneling spectroscopy measurements on these types of films.<sup>13</sup>

In section II we compare the optical properties of bulk Ag films and of Ag QD monolayers, and we describe the contributions expected from both bound and free carriers to the complex dielectric function. In section III we present the experimental

\* Corresponding author. E-mail: heath@chem.ucla.edu.

<sup>†</sup> Department of Chemistry and Biochemistry, UCLA.

<sup>‡</sup> Department of Chemistry, UC Berkeley.

<sup>§</sup> Department of Physics, UC Berkeley.

(1) Kagan, C. R.; Murray, C. B.; Nirmal, M.; Bawendi, M. G. *Phys. Rev. Lett.* **1996**, *76*, 1517.

(2) Shiang, J. J.; Heath, J. R.; Collier, C. P.; Saykally, R. J. *J. Phys. Chem. B* **1998**, *102*, 3425.

(3) Collier, C. P.; Vossmeier, T.; Heath, J. R. *Annu. Rev. Phys. Chem.* **1998**, *49*, 371.

(4) Collier, C. P.; Saykally, R. J.; Shiang, J. J.; Henrichs, S. E.; Heath, J. R. *Science* **1997**, *277*, 1978.

(5) Markovich, G.; Collier, C. P.; Henrichs, S. E.; Remacle, F.; Levine, R. D.; Heath, J. R. *Acc. Chem. Res.* **1999**, *32*, 415.

(6) Stafford, C. A.; Das Sarma, S. *Phys. Rev. Lett.* **1994**, *72*, 3590.

(7) Lambe, J.; Jaklevic, R. C. *Phys. Rev. Lett.* **1969**, *22*, 1371.

(8) Cavicchi, R. E.; Silsbee, R. H. *Phys. Rev. B* **1988**, *37*, 706.

(9) Medeiros-Ribeiro, G.; et al. *Phys. Rev. B* **1998**, *59*, 1633.

(10) Markovich, G.; Collier, C. P.; Heath, J. R. *Phys. Rev. Lett.* **1998**, *80*, 3807.

(11) Davis, C. A.; McKenzie, D. R.; McPhedran, R. C. *Optics Commun.* **1991**, *85*, 70.

(12) Remacle, F.; Levine, R. *J. Am. Chem. Soc.* **2000**, *122*, 4084–4091.

(13) Kim, S.-H.; Medeiros-Ribeiro, G.; Ohlberg, D. A. A.; Williams, R. S.; Heath, J. R. *J. Phys. Chem. B* **1999**, *103*, 10341.

procedure used to measure compression-dependent reflectance ( $R$ ) and transmittance ( $T$ ) spectra. These data were inverted using the Newton–Raphson algorithm<sup>14,15</sup> in order to determine the complex index of refraction,  $n - ik$ , where  $\epsilon(\omega) = (n - ik)^2$ , and this algorithm is described in section IV. Previous workers used a similar technique to describe the optical properties of evaporated (and growing) Ag island films and found it to be unsatisfactory near the percolation threshold.<sup>16</sup> There exist multiple solutions to  $\epsilon(\omega)$  for a given set of  $R$  and  $T$  values, and those solutions are poorly defined when  $n$  and  $k$  are nearly equal, as happens near a MI transition. The result is that the algorithm cannot distinguish between the various solutions, and the fit of the  $R$  and  $T$  measurements to the optical constants is poor. The practice has been to simply choose the most physically meaningful of the possible solutions, and even then, the resulting  $\epsilon(\omega)$  function is not well defined. We avoided this dilemma by using a Kramers–Kronig analysis of the data in conjunction with the inversion technique. This analysis, which is described in section IV, was mathematically rigorous in that it involved no approximations, and it led to a *single* unambiguous solution of  $\epsilon(\omega)$ . In section V, we present our results.

## II. The Optical and Electronic Properties of Silver and Silver Quantum Dots

In a bulk metal, the complex dielectric function, at frequencies from DC to the ultraviolet, is dominated by contributions from free electrons. In this region the real part of the dielectric function,  $\epsilon_1(\omega)$ , has a negative value. At some high frequency, known as the bulk plasmon resonance frequency,  $\epsilon_1(\omega)$  will cross over to positive values. Metals are also characterized by bound (interband) transitions that contribute to the dielectric function, although for most metals the bound transitions are only important at very high frequencies. However, for the one-electron metals, such as silver, both the free and bound electron contributions to the dielectric function are important through the optical and UV frequencies.<sup>17</sup> The free electron contribution to  $\epsilon_1(\omega)$  has a negative value at frequencies below  $\sim 8$  eV, while the interband transitions are characterized by a positive-valued contribution to  $\epsilon_1(\omega)$  at all frequencies, with strong resonant dispersive behavior near 4 eV. When these two components add together, one measures a total  $\epsilon_1$  that has a negative value up to 3.8 eV (the “effective” bulk plasmon  $\omega_p$ ), has a (positive-valued) resonance in the UV, and gradually increases at higher energies.

In isolated silver QDs, the optical and electronic properties are quite different from those of the bulk. Low-frequency conductivity is obviously absent in isolated Ag QDs, which means that  $\epsilon_1(\omega)$  has a positive value at all frequencies. Throughout the optical and near-UV regions of the spectrum,  $\epsilon_1(\omega)$  is dominated by the optically allowed surface plasmon resonance,  $\omega_{sp}$ .  $\omega_{sp}$  describes the collective resonance of the free electrons within an *individual* QD and depends on the bulk dielectric function for Ag, modified for finite size. To a first approximation,  $\omega_{sp} \approx \omega_p(3)^{1/2}$ , although in a superlattice of QDs, classical coupling between adjacent QDs (local field effects), as well as the size of the individual QDs, affects the resonance position.<sup>2</sup> At the MI transition, the dielectric function should be further modified by the addition of significant free

electron density *between* multiple sites within the superlattice, and the result should be an additional negative-valued contribution to  $\epsilon_1(\omega)$ .

The most important distinction between the particle sizes is related to the single-particle, or (super)lattice site charging energies,  $\epsilon_c = e^2/C(r)$ , where  $C(r) = 4\pi\epsilon_0\epsilon_r$ . Here,  $\epsilon$  is the dielectric constant of the organic surface groups that surround the particle,  $r$  is the particle radius, and the other symbols take on their usual meaning. For 3-nm-diameter alkythiol passivated Ag QDs, we have measured a charging energy of about 0.3 eV.<sup>9</sup> It is this charging energy that leads to the Coulomb band gap in the *superlattice* and therefore makes the superlattice a Mott insulator. For a Mott-type MI transition, when the quantum mechanical exchange coupling between the particles exceeds the Coulomb gap, then the system undergoes a transition to the metallic phase.<sup>18</sup> Since the charging energy scales inversely with particle size, the MI transition is experimentally easier to access in superlattices composed of the larger quantum dots. Through the use of a number of experimental approaches (both optical and transport measurements), we have found that for Ag particles in the range of 6–8 nm diameter, the MI transition occurs in the range of  $\delta = 9 \pm 2$  Å, while for 3.0- or 3.5-nm-diameter particles, the MI transition occurs near  $\delta = 6 \pm 2$  Å.<sup>1</sup> Here,  $\delta$  is the separation between the surfaces of the Ag cores of adjacent QDs. In addition, we have found that order in the superlattice is *qualitatively* less important for larger particles. When a monolayer collapses to a bilayer, the bilayer structure is characterized by a higher entropy than the monolayer.<sup>19</sup> Microscopic inspection of a collapsed film reveals that the bilayer structure is, indeed, much more disordered than that of the monolayer. We have never observed the MI transition in a collapsed monolayer of 3.0- or 3.5-nm-diameter particles, while the transition is readily observed in collapsed monolayers of 6- or 8-nm particles. It could be that the spread in lattice site energies that arises from local chemical environments is smaller for larger particles.

## III. Experimental Section

There are many methods for determining the optical constants of a sample, including ellipsometry, polarimetry, and multiple oblique angle of incidence measurements at different polarizations.<sup>20</sup> Most involve multiple *consecutive* measurements. This works well with a sample that does not change during the time it takes to complete the measurements. However, Langmuir monolayers of Ag QDs each have sufficiently different optical properties that *simultaneous* measurements on a single film during compression were necessary. Because of the limited amount of space available in the Langmuir trough and the relative simplicity of the calculations in this geometry, we found that it was best to measure the transmittance and reflectance at normal incidence as a function of trough area.

The experimental setup is shown in Figure 1. White light from a 150-W tungsten/halogen lamp was coupled to the Langmuir trough through a 400- $\mu$ m-diameter glass fiber optic. The light exiting this fiber was collimated and sent through a pinhole, which restricted the diameter of the light spot on the film to less than 1 mm. A color process filter (Schott, BG37) was used to balance the spectral intensity of the lamp. The light then passed through a 50/50 beam splitter and was directed onto the thin film. The light reflected from the film was reflected from the beam splitter a second time and collected with another fiber optic. A third fiber optic was immersed in the water subphase beneath the film to measure changes in transmittance. It was necessary to make a

(14) Heavens, O. S. *Optical Properties of Thin Solid Films*; Butterworth Scientific Publications: London, 1955; Section 4.9, pp 76–77.

(15) Nilsson P. O. *Appl. Opt.* **1968**, 7, 435.

(16) Rouard P.; Meesen, A. In *Progress in Optics*; Wolf, E., Ed.; North-Holland: Amsterdam, 1977; Vol. 15, p 79, and references therein.

(17) Bohren C. F.; Huffman, D. R. *Absorption and Scattering of Light by Small Particles*; John Wiley & Sons: New York, 1983.

(18) Mott, N. F. *Metal–Insulator Transitions*; Taylor & Francis Ltd.: London, 1990.

(19) Heath, J. R.; Knobler, C. M.; Leff, D. V. *J. Phys. Chem.* **1997**, 101, 189.

(20) Ward, L. *The Optical Constants of Bulk Materials and Films*, 2nd ed.; Institute of Physics Publishing: Bristol, 1994.

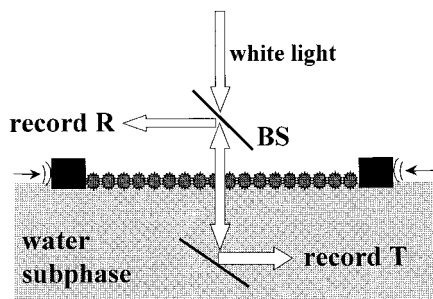


**Figure 1.** Schematic diagram of the experimental setup for measuring the reflectance and transmittance of a QD film as a function of compression on the Langmuir trough. A white light source is sent toward the air/water interface. The reflected portion is split off with a beam splitter (BS), and the reflectance spectrum is collected using a multichannel array detector. The transmitted portion is reflected off a mirror at the bottom of the trough, and the transmittance spectrum is collected on a second array detector. Pressure/area isotherms are collected simultaneously with these measurements.

tiny “mirror” from a slice of a small steel ball bearing in order to couple enough light into this transmission fiber, since it was directed perpendicularly to the incident beam. All immersed components were cleaned with chloroform between experiments.

The reflection and transmission fibers were connected to two identical, fiber-coupled UV–vis spectrometers (Ocean Optics). Three computers were used to collect the simultaneous transmission and reflection spectra and the surface pressure/area isotherm. The spectral ranges that gave acceptable signal-to-noise ratios were 388–775 and 860–950 nm.

Prior to carrying out a set of measurements for a particular film, we collected two sets of control *R* and *T* spectra. The first set was simply a measurement of the dark counts on both spectrometers, and this was subtracted from all subsequently collected data sets. The second was a measurement of the *R* and *T* spectra of the water subphase without the particle monolayer. Because the refractive index of water is well known throughout the wavelength range studied here, this measurement could be used to calibrate the spectrometers and the light sources, as well as to subtract the contribution of the water subphase to the *R* and *T* values measured when a QD monolayer was present. Accurate values for the percent reflectance and transmittance of the QD films were calculated by normalizing the collected spectra against similarly collected spectra for pure water.<sup>21</sup>

Details of the Ag QD synthesis and the formation and compression of superlattices of these particles on a Langmuir trough are found elsewhere.<sup>18,22</sup> All particles utilized here were size-selected to produce distributions with widths of 10% or less. The thickness of the Langmuir film is simply related to the diameter of the nanoparticles and the number of layers (1 or 2) in the film. The particle diameters were determined from transmission electron microscopy (TEM) or from the frequency of the maximum of the surface plasmon (Mie) resonances of the particles in solution. These resonances were calibrated with TEM measurements and X-ray diffraction.

The results from the compression of two films are presented here, although similar results were observed for several other films. Film 1 consisted of 8-nm-diameter particles capped with decanethiol, and film 2 consisted of 6-nm-diameter particles capped with hexanethiol. Figure 2 shows the reflectance, transmittance, and surface pressure measurements as a function of trough area for film 2.

#### IV. Optical Constants by the Newton–Raphson Method

The results for  $R_{\text{film}}$  and  $T_{\text{film}}$  at normal incidence were inverted by computer to obtain optical constants,  $n$  and  $k$ , where  $\epsilon(\omega) = (n - ik)^2$ . We used an approach appropriate for a three-

layer system when multiple reflections in the thin film must be taken into account.<sup>14,15</sup> The system consists of three media. The first is the air, characterized by a real index of refraction,  $n_0$ . The second medium is the quantum dot thin film, characterized by a thickness,  $d$ , and by a complex index of refraction,  $n(\omega) - ik(\omega)$ . The third medium is the water subphase of the Langmuir trough, which has a real index of refraction,  $n_2(\omega)$ <sup>17</sup> (we assume  $k_2 = 0$  at these wavelengths). For this model, the reflectance and transmittance may be found from the following system of equations:

$$g_1 = \frac{n_0^2 - n^2 - k^2}{(n_0 + n)^2 + k^2} \quad (1)$$

$$h_1 = \frac{2n_0k}{(n_0 + n)^2 + k^2} \quad (2)$$

$$g_2 = \frac{n^2 - n_2^2 + k^2}{(n + n_2)^2 + k^2} \quad (3)$$

$$h_2 = \frac{2(n_2k)}{(n + n_2)^2 + k^2} \quad (4)$$

$$A = 2(g_1g_2 + h_1h_2) \quad (5)$$

$$B = 2(g_1h_2 - h_1g_2) \quad (6)$$

$$C = 2(g_1g_2 - h_1h_2) \quad (7)$$

$$D = 2(g_1h_2 + h_1g_2) \quad (8)$$

$$\alpha_1 = \frac{\omega}{c}dk \quad \gamma_1 = \frac{\omega}{c}dn \quad (9)$$

$$R_{\text{film}} = \frac{(g_1^2 + h_1^2)e^{2\alpha_1} + (g_2^2 + h_2^2)e^{-2\alpha_1} + A \cos 2\gamma_1 + B \sin 2\gamma_1}{e^{2\alpha_1} + (g_1^2 + h_1^2)e^{-2\alpha_1} + C \cos 2\gamma_1 + D \sin 2\gamma_1} \quad (10)$$

$$T_{\text{film}} = \frac{n_2}{n_0} \frac{((1 + g_1)^2 + h_1^2)((1 + g_2)^2 + h_2^2)}{e^{2\alpha_1} + (g_1^2 + h_1^2)e^{-2\alpha_1} + C \cos 2\gamma_1 + D \sin 2\gamma_1} \quad (11)$$

In Figure 3 we present a contour plot of the reflectance and transmittance as a function of  $n$  and  $k$ . The intersections of the contours represent solutions to eqs 10 and 11 for a set of reflectance and transmittance values. The first point to note is that there are multiple solutions to this system of equations. Fortunately, we can generally use the thickness of our films to eliminate all but two solutions to the data. However, those two solutions are not similar to each other. Without any other evidence (such as the results of the Kramers–Kronig analysis presented below), one cannot be sure which solution is correct, and one must resort to using physical intuition when choosing a solution. The second point is that in the region of the graph where  $n = k$ , the contours are roughly tangential to each other. In these regions, the algorithm will not resolve accurate values for  $n$  and  $k$ . This is because there is a large range of  $n$  and  $k$  values that will produce the same  $R$  and  $T$  values within the precision of the calculation. This problem is not unique to our system and has similarly plagued measurements of the dielectric function of evaporated Ag islands as they are grown through

(21) Schiebener, P.; Straub J.; Levelt-Sengers, J.; Gallagher, J. S. *J. Phys. Chem. Ref. Data* **1980**, *19*, 677.

(22) Korgel, B. A.; Fullam, S.; Connolly, S.; Fitzmaurice, D. *J. Phys. Chem. B* **1998**, *102*, 8379.



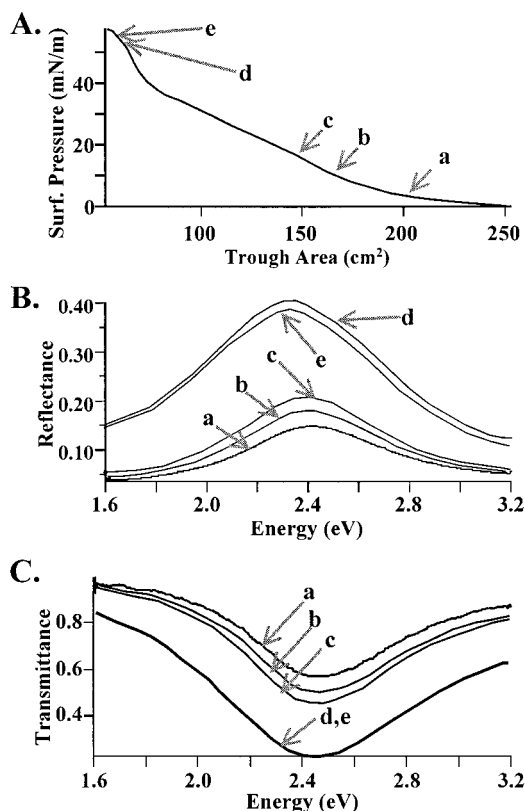


**Figure 2.** Experimental results for the film comprised of 6-nm silver QDs (film 2). Isotherm A shows that the film began to collapse at an area of about 140 cm<sup>2</sup> and formed a continuous bilayer at about 65 cm<sup>2</sup>. Reflectance (B) and transmittance (C) data were used only from the regions where the film was a continuous monolayer (points a, b) (6 nm thick) or bilayer (points c–e) (12 nm thick), where the thickness of the film was certain. The reflectance was observed to increase steadily upon compression until the MI transition was reached (60 cm<sup>2</sup>), at which point it dropped (curve e), while the transmittance dropped steadily until the transition, after which it did not change much (curve e superimposes onto curve d).

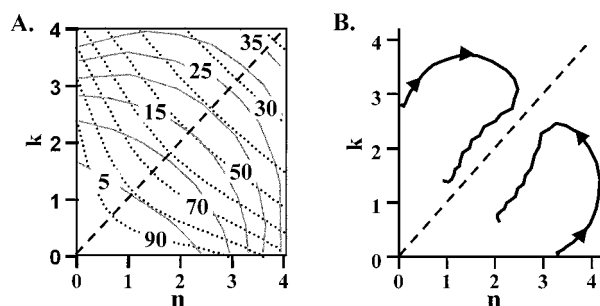


**Figure 3.** (A) Representative contour plot of the reflectance (*R*) (dotted lines) and transmittance (*T*) (solid lines) as a function of *n* and *k* for film 2 in the visible wavelength range. The curves are labeled according to %*T* or %*R*. Close to *n* = *k* (dashed line), the *R* and *T* contours are nearly parallel, and this causes large errors in the computer determination of the dielectric function solution to this system of equations. (B) The computer fits of the data from film 2, as a compressed continuous bilayer, to the *R* and *T* equations. Arrows indicate the direction of increasing frequency. Both solutions are shown, and a clear change in the curve is seen when the solutions approach the region parallel to *R* and *T* contours. A decrease in the quality of the fit to the data is also observed in this region.

the percolation transition.<sup>16</sup> The quality of the solutions is checked by entering the *n* and *k* values back into the *R* and *T* equations and comparing the results to the data. Although a very good solution (it matches to several decimal places) may

be found in the *n* = *k* region of the contour plot, the error is usually at least an order of magnitude worse than in the region far from the *n* = *k* line. To obtain more precise values for the optical constants in this region, another complementary method of analysis is needed.

## V. Kramers–Kronig Analysis

For this section, we adapted a well-known variation of the Kramers–Kronig dispersion relations with some slight modifications. The Kramers–Kronig relations are based on the principle of causality.<sup>23</sup> Given a complex function that represents a physical system, the real part can be represented by an integral expression involving the imaginary part, and the imaginary part can be represented as an integral expression involving the real part. The expression that is relevant here relates the relative phase,  $\theta(\nu_0)$ , of the transmitted light, as a function of frequency, to the transmittance,  $T(\nu_0)$ , through the sample.<sup>15</sup>

$$\theta(\nu_0) = \frac{2\nu_0}{\pi} \int_0^\infty \frac{\ln \sqrt{T(\nu)}}{\nu^2 - \nu_0^2} d\nu - 2\pi\nu_0 d \quad (12)$$

Appropriate units must be used for the frequency and thickness so that  $\theta$  is unitless. After the phase is determined from the transmittance data, both of these values are fit to equations that relate the real and imaginary parts of the refractive index (*n* and *k*, respectively) to the transmittance and phase as a function of wavelength,  $\lambda$ .<sup>14</sup>

$$T(\lambda) = \frac{16(n^2 + k^2)}{C(\lambda)^2 + D(\lambda)^2} \quad (13)$$

$$\theta(\lambda) = \arctan \left[ \frac{kC(\lambda) + nD(\lambda)}{kD(\lambda) + nC(\lambda)} \right] \quad (14)$$

where the functions  $C(\lambda)$  and  $D(\lambda)$  are different from eqs 7 and 8,

$$C(\lambda) = \left[ e^{2\pi k d / \lambda} \left\{ \left[ (1+n)(n+n_s) - k^2 \right] \cos \left( \frac{2\pi n d}{\lambda} \right) + k(1+2n+n_s) \sin \left( \frac{2\pi n d}{\lambda} \right) \right\} + e^{-2\pi k d / \lambda} \left\{ \left[ (1-n)(n-n_s) + k^2 \right] \cos \left( \frac{2\pi n d}{\lambda} \right) - k(1-2n+n_s) \sin \left( \frac{2\pi n d}{\lambda} \right) \right\} \right] \quad (15)$$

$$D(\lambda) = \left[ e^{2\pi k d / \lambda} \left\{ \left[ (1+n)(n+n_s) - k^2 \right] \sin \left( \frac{2\pi n d}{\lambda} \right) + k(1+2n+n_s) \cos \left( \frac{2\pi n d}{\lambda} \right) \right\} + e^{-2\pi k d / \lambda} \left\{ \left[ (1-n)(n-n_s) + k^2 \right] \sin \left( \frac{2\pi n d}{\lambda} \right) - k(1-2n+n_s) \cos \left( \frac{2\pi n d}{\lambda} \right) \right\} \right] \quad (16)$$

Here,  $n_s$  is the index of refraction of the sample substrate and may be a function of wavelength.

In principle, one can determine the optical constants from a single measurement, but, as is apparent from eq 12, one needs to know the transmittance over *all* frequencies in order to

(23) Arfken, G. B.; Weber, H. J. *Mathematical Methods for Physicists*; Academic Press: San Diego, CA, 1995; p 444.

determine the phase shift at a given frequency. The simplest solution to this problem is to collect data over the largest frequency range possible and to extrapolate the data in the regions where no data are available. Significant errors can result if the data are limited to a small frequency range or if there are spectral features outside of the measured frequency range. A mathematically exact solution to this problem exists if there are other data available that provide the optical constants for at least two frequencies. In our case, these additional data are determined from the reflectance data. The application of the mean value theorem for integrals to the Kramers–Kronig relation has been previously described,<sup>24</sup> but since the detailed expressions used in the present study differ slightly from those used by others, the derivation will be summarized below.

First, there is a singularity in eq 12 when  $\nu = \nu_0$  that causes problems with numerical integration. This problem is solved by subtracting the expression

$$\int_0^\infty \frac{\ln\sqrt{T(\nu_0)}}{\nu^2 - \nu_0^2} d\nu = 0 \quad (17)$$

from eq 12. The above integral is analytic (single valued) and continuous interior to and on a closed simple contour bounded by the real and imaginary frequency axes in the upper half of the complex plane.<sup>15</sup> Since there is a pole on the  $Re \omega$  axis that can be avoided by applying an infinitesimal semicircle at  $\omega = \omega_0$ , there are no enclosed residues. The residue theorem,  $\oint_C f(z) dz = 2\pi i \sum(\text{enclosed residues})$ , applies, and the integral in eq 17 will vanish.<sup>25</sup> When eq 17 is subtracted from eq 12, the result is

$$\theta(\nu_0) = \frac{2\nu_0}{\pi} \int_0^\infty \frac{\ln\sqrt{T(\nu)} - \ln\sqrt{T(\nu_0)}}{\nu^2 - \nu_0^2} d\nu - 2\pi\nu_0 d \quad (18)$$

This ensures that the singularity found in eq 12 can be avoided without changing the value of the integral. Velický<sup>26</sup> first showed a general proof for this result, which involved expanding the denominator of the integrand in eq 18 above as a power series, substituting this series back into eq 18, and taking the limit as  $\omega$  approaches infinity.

Next, the frequency range is divided into three regions:<sup>27</sup> (0,  $a$ ) is zero frequency to the beginning of the data range, ( $a$ ,  $b$ ) is the frequency range of the data, and ( $b$ ,  $\infty$ ) is from the end of the data to infinity. Equation 12 then becomes

$$\theta(\nu_0) = \Phi 1(\nu_0) + \Phi 2(\nu_0) + \Phi 3(\nu_0) \quad (19)$$

where

$$\Phi 1(\nu_0) = \frac{2\pi}{\nu_0} \left[ \int_b^\infty \frac{\ln\sqrt{T(\nu)}}{\nu^2 - \nu_0^2} d\nu - \int_0^a \frac{\ln\sqrt{T(\nu_0)}}{\nu^2 - \nu_0^2} d\nu \right] \quad (20)$$

$$\Phi 2(\nu_0) = \frac{2\nu_0}{\pi} \int_a^b \frac{\ln\sqrt{T(\nu)} - \ln\sqrt{T(\nu_0)}}{\nu^2 - \nu_0^2} d\nu - 2\pi\nu_0 d \quad (21)$$

$$\Phi 3(\nu_0) = \frac{2\pi}{\nu_0} \left[ \int_b^\infty \frac{\ln\sqrt{T(\nu)}}{\nu^2 - \nu_0^2} d\nu - \int_b^\infty \frac{\ln\sqrt{T(\nu_0)}}{\nu^2 - \nu_0^2} d\nu \right] \quad (22)$$

$\Phi 2$  can be evaluated numerically on the computer, but since  $\Phi 1$  and  $\Phi 3$  involve frequencies where no data is available, they must be manipulated further. The second integral in these expressions is found in a table of integrals,<sup>28</sup> and the first integral is integrated by parts twice to obtain for  $\Phi 1$

$$\Phi 1(\nu_0) = -\frac{1}{\pi} \int_0^a \ln\sqrt{T(\nu)} \frac{d}{d\nu} \ln \left| \frac{\nu + \nu_0}{\nu - \nu_0} \right| d\nu + \frac{\ln\sqrt{T(\nu_0)}}{\pi} \ln \left| \frac{a + \nu_0}{a - \nu_0} \right| \quad (23)$$

The mean value theorem for integrals is applied to the first integral to get

$$\Phi 1(\nu_0) = A \ln \left| \frac{a + \nu_0}{a - \nu_0} \right| + \frac{\ln\sqrt{T(\nu_0)}}{\pi} \ln \left| \frac{a + \nu_0}{a - \nu_0} \right| \quad (24)$$

$$A = -\frac{\ln\sqrt{T(\xi)}}{\pi}$$

where  $\xi$  is some frequency between zero and  $a$ . Similarly for  $\Phi 3$ :

$$\Phi 3(\nu_0) = B \ln \left| \frac{b + \nu_0}{b - \nu_0} \right| - \frac{\ln\sqrt{T(\nu_0)}}{\pi} \ln \left| \frac{b + \nu_0}{b - \nu_0} \right| \quad (25)$$

$$B = \frac{\ln\sqrt{T(\eta)}}{\pi}$$

where  $\eta$  is some frequency between  $b$  and infinity. Since  $T$  is between 0 and 1, it is clear from eqs 24 and 25 that  $A$  must be positive and  $B$  negative, but the exact values of these constants must be determined from some additional data.  $A$  and  $B$  may be determined uniquely by realizing that the measured phase shift,  $\Phi 2(\nu_0)$ , is zero at frequencies below an absorption.<sup>24</sup> If  $\Phi 2(\nu_0)$  vanishes, at least at two frequencies in the interval ( $a$ ,  $b$ ), for example, at  $\nu = c$  or  $\nu = d$ , then  $A$  and  $B$  can be determined from the following pair of simultaneous equations:

$$A \ln \left| \frac{a + c}{a - c} \right| + \Phi 2(c) + B \ln \left| \frac{b + c}{b - c} \right| = 0 \quad (26a)$$

$$A \ln \left| \frac{a + d}{a - d} \right| + \Phi 2(d) + B \ln \left| \frac{b + d}{b - d} \right| = 0 \quad (26b)$$

Equations 26a and 26b show clearly that  $\nu_0$  should not be evaluated at the endpoints  $a$  and  $b$  to avoid singularities there. Additionally, although this analytical technique is mathematically exact and, hence, may extend the frequency range over which the optical constants can be determined, small errors in the data are amplified into large errors in the optical constants near the endpoints of the data and should not be trusted there. The quality of the results is determined by comparing the reflectance calculated from the optical constants to the reflectance data that were collected. For the results presented here, the phase shift was obtained from values of  $n$  and  $k$  determined from the  $R$  and  $T$  fits at frequencies where the  $n$  and  $k$  values are most certain (in the red region of the spectrum).

(28) CRC integral tables.

(24) Roessler, D. M. *Br. J. Appl. Phys.* **1965**, *16*, 1119.

(25) Arfken, G. B.; Weber, H. J. *Mathematical Methods for Physicists*; Academic Press: San Diego, CA, 1995; p 415.

(26) Velický, B. *Czech. J. Phys. B* **1961**, *11*, 787.

(27) Stern, F. In *Solid State Physics*; Seitz, F., Turnbull, D., Eds.; Academic: New York, 1963; Vol. 15, p 299.

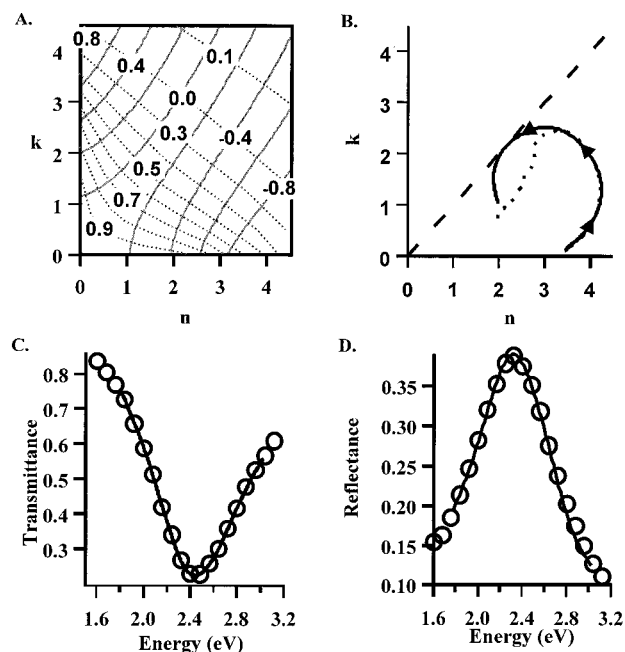


**Figure 4.** (A) Representative contour plot of the % transmittance (dotted line) and phase (solid line) as a function of  $n$  and  $k$  for a 12-nm-thick film in the visible wavelength range. The unitless value of phase is described by eq 19 in the text. (B) The results of the Kramers–Kronig calculation (solid line) compared to the result of the  $R$  and  $T$  inversion for the compressed continuous bilayer data from film 1. The discontinuity in the data near the  $n = k$  line is not present in the Kramers–Kronig result. (C) Calculated transmittance (solid line) from the Kramers–Kronig optical constants compared to the original data (circles). (D) Similar comparison of the reflectance data. The Kramers–Kronig results are unreliable near the endpoints of the data.

A contour plot of  $T$  and  $\theta$  as a function of  $n$  and  $k$  is shown in Figure 4A. As with the  $R$  and  $T$  functions, there are generally multiple combinations of  $n$  and  $k$  that will reproduce the data, *but only the correct solution will appear in both the methods of determining the optical constants*. Fortunately, because the films we examine here are so thin, only one solution falls within the physically acceptable bounds of  $n$  and  $k$ . In addition, the  $T$  and  $\theta$  contours are orthogonal to each other, so there is no ambiguity in the solution for the optical constants. Figure 4B shows a representative result of the  $n$  and  $k$  calculation with a comparison to the  $R$  and  $T$  inversion result. The Kramers–Kronig result produces a much more precise value of  $n$  and  $k$  in the region of the contour plot where  $n = k$  and reproduces the experimental data very well (Figure 4C,D). For all data sets, only a single solution satisfied both the  $R$  and  $T$  inversion and the Kramers–Kronig analysis, showing that a combination of the  $R$  and  $T$  inversion and the Kramers–Kronig analysis allows for the unambiguous determination of the optical constants over the entire experimental range of frequencies.

## V. Results and Discussion

There are several ways to present  $\epsilon(\omega)$ , and perhaps the simplest is known as a Cole–Cole plot.<sup>29</sup> For such a plot, the  $x$ - and  $y$ -axes are  $\epsilon_1$  and  $\epsilon_2$ , respectively, and the points on the plot correspond to different frequency values. Because the spectral region that we measured is dominated by  $\omega_{\text{sp}}$ , the plots form a circular arc, with frequency increasing counterclockwise around the arc.

In Figure 5A we present Cole–Cole plots for the 6-nm nanocrystal Langmuir monolayer at relatively low compression.

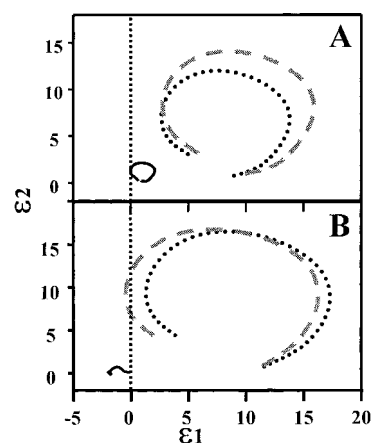


**Figure 5.** Plots of the real versus the imaginary parts of the dielectric function for a Langmuir monolayer of 6-nm-diameter Ag nanocrystals as various compressions. In part A, we present results for the case in which an insulating film is compressed. The dotted curve represents the film at  $1.2 \times 10^4 \text{ \AA}^2/\text{particle}$ , while the dashed-line curve represents the film at  $0.9 \times 10^4 \text{ \AA}^2/\text{particle}$ . The solid-line curve represents the difference and indicates that only bound states contribute to the observed changes in optical properties. In part B, the changes observed when the superlattice becomes metallic are shown. The film is compressed by a small fraction ( $\sim 2\%$ ), and the plot shifts to the left. The difference between these curves is characterized by a negative value  $\epsilon_1$  at all measured frequencies and indicates a free electron contribution to the dielectric function.

The film represented by the dotted-line trace was compressed by about 25% (in area) to yield the dashed-line trace. The solid trace represents the difference between the films. This difference tells us that the optical properties have not changed much—the resonance has just gotten stronger, mostly due to an increased density of particles on the trough surface. This is typical for compressions up to the MI transition. In Figure 5B we present Cole–Cole plots corresponding to the same film at higher compressions. The film characterized by the dashed-line circle was compressed by about 2% from the dotted-line circle. The difference between these plots is characterized by a negative-valued  $\epsilon_1(\omega)$  at all measured frequencies. This is the signature that corresponds to the onset of free electron behavior within the superlattice, which is the MI phase transition.

In the accompanying paper, Remacle and Levine discuss the implications of disorder in these films.<sup>12</sup> They calculate that there are *two* quantum phase transitions that might be observed as a monolayer is compressed. The first corresponds to the disappearance of the Coulomb gap and is a Mott-type MI transition. However, if the system is disordered, it will not exhibit metallic character at that point but will be an insulator due to localization effects (so-called Anderson localization). Only upon further compression does the system become truly metallic. In Figure 6 we present evidence for this localized phase. In this case the uncompressed film of 8-nm particles (film 1) was already metallic, indicated by the fact that  $\epsilon_1(\omega)$  has a negative value over much of the measured frequency range. *This means that this monolayer has metallic character even when the particles are at their equilibrium separation distance ( $\sim 9 \text{ \AA}$ ).* As discussed above, and as previously demonstrated,<sup>19</sup> a bilayer is characterized by higher entropy than the monolayer, and so collapsing a monolayer provides a mechanism for increasing disorder in the system. In Figure 6A, we show that when the monolayer (dotted curve) collapses to form a bilayer (dashed-line curve), the Cole–Cole plot shifts sharply to the right. The difference between these two curves (solid trace) is a relative enhancement of the contribution of the bound

(29) Cole, K. S.; Cole, R. H. *J. Chem. Phys.* **1941**, 9, 341.

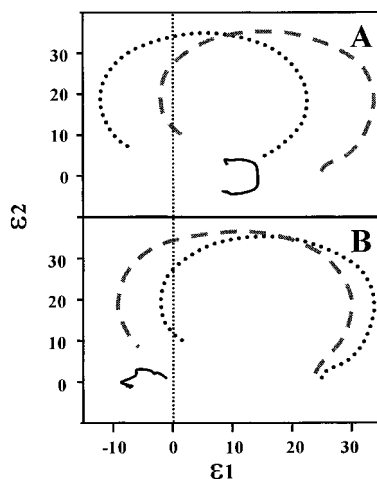


**Figure 6.** Cole–Cole plots demonstrating the importance of disorder on the free electron contribution to the dielectric function. In A, a metallic monolayer (dotted trace) is collapsed into a disordered bilayer (dashed-line trace), and the difference between the two films (solid trace) is a relative enhancement of the bound resonances to the optical response. In B, the collapsed bilayer is further compressed and becomes metallic again. The measured difference is a purely free electron contribution.

transitions. Upon further compression, we observe a transition back to the metallic state (Figure 6B). This observation indicates that the optical properties, while sensitive probes of free electron behavior, are not sensitive to the presence or absence of a Coulomb band gap.

## Conclusions

We have reported on the first quantitative measurements of the insulator-to-metal quantum phase transition in metal quantum dot superlattices. The complex dielectric function of organically passivated silver quantum dot monolayers was measured as a function of interparticle separation distance. An experimental technique for the simultaneous measurement of reflectance and transmittance data in quantum dot Langmuir monolayers was

described, and we have presented algorithms for extracting the complex dielectric function of those monolayers from the measurements. In particular, we have demonstrated how such algorithms may be used even in the region where  $n$  and  $k$  are approximately equal and standard Newton–Raphson matrix inversion techniques do not resolve to a satisfactory solution. When these algorithms are applied to the analysis of transmittance and reflectance data taken from silver quantum dot monolayers as they are compressed through the metal/insulator transition, unambiguous signatures corresponding to the onset of free electron response are observed. Both the experimental technique and the algorithms utilized here should be useful for measuring the dielectric function of both monolayer and multilayer metal and semiconductor quantum dot superlattices, and for quantifying the classical and/or quantum nature of interparticle exchange coupling in those films.

In these measurements, the “total”  $\epsilon_1(\omega)$  has a negative value only at high frequencies. Based on the low-frequency measurements,<sup>10</sup>  $\epsilon_1(\omega)$  must at some point cross from a positive to a negative value between 10 MHz and the low-frequency limit of the measurements reported here. That crossover (possibly in the infrared) represents a collective resonance of the superlattice that appears only at the onset of metallic behavior. It would be interesting to extend these measurements toward longer wavelengths. When these films become metallic, the electrons are delocalized, but the positive cores are still obviously localized. The collective resonance that appears at the MI transition should contain information relevant to the free electron density in these unusual metallic films.

**Acknowledgment.** We acknowledge support from an NSF-GOALI grant, the Semiconductor Research Corporation, and the Sloan Foundation, as well as helpful discussions with Raphael Levine, Françoise Remacle, Sang-Ho Kim, and Stan Williams. S.H., C.P.C., and J.R.H. contributed equally to this work.

JA991543F